Saturable Absorption of Few-layer WS$_2$ and WSe$_2$ at Exciton Resonance

Shuang Liang[1], Yuze Lu[1], Haimu Liu[1], Xiaohe Shang[1], Rongguang Du[1], Jiamin Ji[1], Yiling Yu[1], and Shunping Zhang[1, 2, *]

[1]School of Physics and Technology and Key Laboratory of Artificial Micro- and Nano-structures of Ministry of Education, Wuhan University, Wuhan 430072, China.

[2]Wuhan Institute of Quantum Technology, Wuhan 430206, China.

Abstract

Layered materials such as graphene and transition metal dichalcogenides (TMDs) are excellent candidates as saturable absorbers. However, the saturable absorption of few-layer TMDs is usually measured at the typical wavelengths of lasers, away from the exciton resonances. In this work, we study the saturable absorption effects in one, two, and three-layer WS$_2$ and WSe$_2$, around the A-exciton resonance, using a tunable pulsed laser. Power-dependent reflectance contrast indicates that the saturation power density thresholds are around 5.5×10^6 W/cm^2 (3.8×10^6 W/cm^2) for monolayer WS$_2$ (WSe$_2$), showing an order of magnitude reduction at the exciton peak. The saturation power density threshold increases with the number of layers. The analytical solution to the dynamics equation illustrates how the laser parameters influence the experimentally measured threshold, highlighting the importance of pulse duration in saturable absorption. This result reveals the

effect of exciton decay and exciton-exciton interactions on the nonlinear optical properties of TMDs and benefits the design of TMD-based active optical devices.

1. Introduction

Atomically thin two-dimensional materials, including graphene and transition metal dichalcogenides (TMDs), etc., have attracted significant attention due to their exceptional optical and electronic properties [1-5], including their nonlinear optical (NLO) effects [6]. The use of graphene as a saturable absorber is demonstrated as early as 2009 [7]. Known for its low saturation intensity, ultrafast recovery time, and broad tunability, graphene shows promise in applications like mode-locking in fiber lasers [8-14], active control of photonic devices [15-17]. Following this trajectory, the study of nonlinear optics in other layered 2D materials has gained traction over the past decade [18, 19]. For example, the saturable absorption (SA) effects in MoS_2 nanosheets were reported in 2013 [20] and subsequent experiments reveal that few-layer TMDs, such as MoS_2 [21-26], $MoSe_2$ [23, 25, 27], WS_2 [21, 24, 25, 28, 29], and WSe_2 [21, 25, 30], offer superior saturable absorption compared to graphene under similar conditions.

Typically, SA and two-photon absorption responses were reported using z-scan measurements [20-24, 30]. However, different studies used different experimental setups, laser parameters, and sample preparation methods (e.g.,

mechanical exfoliation, liquid-phase exfoliation, and chemical vapor deposition), making it less straightforward to compare the NLO behaviors across different TMDs. More importantly, most reports have focused on z-scan measurements at typical laser wavelengths (800 nm, 632.8 nm, 520 nm, 1550 nm, etc.) [20, 24, 31-33], leaving SA or two-photon absorption at wavelengths near the exciton resonances largely unexplored. Apart from studies utilizing monochromatic lasers, transient absorption spectroscopy using broadband probe light has also been employed to investigate the broad spectral response of TMDs beyond specific wavelengths of typical lasers, uncovering exciton dynamics [34-37] and various NLO responses like bleaching, shifting, and photoinduced bandgap renormalization within the range of A exciton resonance [34, 36, 38-40]. These experimental findings have been further elucidated through theoretical models, considering phase-space filling and Coulomb screening effects, particularly in explaining the bleaching effect at exciton resonant peaks under high-power laser exposure [41-43]. Despite the use of a broadband probe light, transient absorption typically uses a pump beam with a specific wavelength. The saturable absorption at exciton resonant wavelengths, which characterizes the power-dependent NLO response of excitons, including the dynamics of exciton generation, dephasing, and exciton-exciton interaction, remains unexplored.

In this study, we conduct a comprehensive analysis of SA in few-layer WS_2 and WSe_2, around the A exciton resonance, using a pulsed supercontinuum laser. By scanning the pumping wavelengths near the A exciton, we demonstrate the evolution of the saturation power density for different excitation wavelengths, material types, and number of layers.

Notably, both WS_2 and WSe_2 showed significant decreases in reflectance contrast at the A exciton resonance, as the pump power densities increased, indicative of a strong saturable absorption behavior in few-layer TMDs. We observed that the saturation power density threshold for both materials lies between 5.5×10^6 W/cm^2 – 2.12×10^7 W/cm^2, marking an order of magnitude reduction at the exciton peak. Furthermore, the saturation power density is found to increase with the number of layers. Through analytical solutions of the exciton dynamics equation, we investigate the ultrafast behavior exciton density under varying pulse durations, highlighting the critical influence of pulse duration on the saturation threshold and the material's nonlinear optical properties. This result reveals the properties of exciton-exciton interaction in TMDs and benefits the design of TMD-based nonlinear optic devices.

2. Results & discussion

To characterize the SA of few-layer TMDs, we perform power-dependent reflectance contrast measurement under ambient conditions (Fig. 1a). First, the steady reflectance contrast of the samples was obtained using a halogen lamp source. The resonant position of the A exciton was identified by analyzing the broad-spectrum reflectance contrast response of the materials. Then, a supercontinuum laser source (NKT Photonics SuperK Extreme) in conjunction with acousto-optic tunable filters (AOTF) was used to select the wavelength around the A exciton with an FWHM of approximately 3 nm. The repetition rate and pulse duration of the laser source are 8.861 MHz and 78 ps, respectively. The peak power density of our pulsed laser is in the range of $\sim 10^4$ W/cm^2 –10^7 W/cm^2, significantly below the laser peak power density

damage thresholds of the optical lens and that of few-layer TMDs (0.5 GW/cm^2 –1 GW cm^2)[21, 44]. Since the laser is linearly polarized, the pumping power can be precisely adjusted by combining a polarizer and a half-wave plate mounted on a motorized rotational motor (Thorlabs PRM1Z8), without introducing distortion to the beam profile. Real-time power was monitored by splitting a portion of the laser beam into a power meter using a quartz plate. The sample, placed on a piezo stage (Thorlabs MAX313D), was moved into or outside the focus laser spot to repeat the reflection measurements 20 times. The measurement spanning a wide range of power levels and wavelengths, was implemented by a homemade control program that sequentially tuned the angle of the half-wave plate and the wavelength selection of the AOTF. The spot size on the sample was focused to a diameter close to the diffraction limit using an objective lens (Olympus NA = 0.8, 100 ×). The reflected light was collected by the same objective and deflected by a beam splitter to a spectrometer equipped with a CCD camera (HORIBA iHR 550).

Fig. 1b schematically illustrates the generation of exciton complexes with the increasing pump intensity. In the regime of low power density excitation, the optical properties of the TMDs are dominated by the exciton. As the pump power density increases, the interaction between excitons increases, and new quasi-particles such as trion, biexciton, etc. emerge [34]. SA appears due to the phase-space filling effect originating from the Pauli blocking. If the power density goes even higher, a phase transition to plasma state or exciton liquid comes up such that the nonlinear optical response becomes significant.
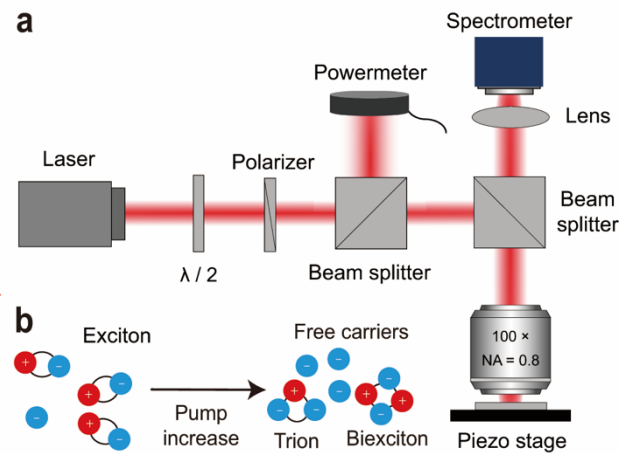
Fig. 1. (a) The schematic of the experimental setup. (b) Schematic of the generation of free carriers, exciton, trion, biexciton, etc., when the pump power increases.

Few-layer TMD samples are mechanically exfoliated from bulk crystals (HQ graphene) by scotch tape [45] and are transferred by PDMS stamp [46] onto quartz substrates. The thickness of atomic thin layers was first identified by their optical contrast under a microscope with verification by atomic force microscope (not shown), PL intensity, and Raman spectroscopy after all the optical measurements. PL and Raman spectra are shown in Fig. 2 with the excitation wavelength of 532 nm. Strong emission is observed at the energy corresponding to A excitonic resonance, which is ~612 nm and ~747 nm for 1L WS_2 and WSe_2, respectively. For WS_2, as the layer number increases to 2L and 3L, the A exciton emission peak decreases by approximately an order of magnitude compared to the 1L sample, consistent with previous work [47]. Photoluminesence corresponding to indirect transition appears in the 2L and 3L samples at ~715 nm and ~790 nm, respectively, which is also consistent with previous reports [48]. Similarly, the A exciton emission peak similarly

reduces significantly when increasing the layer number of WSe$_2$ from 1L to 3L. Indirect luminescence is observed at ~800 nm in 2L samples and ~845 nm in 3L samples, also consistent with previous reports [48]. Figure 2c and 2d show the major Raman peaks of the samples, consistent with previous measurements [47, 48]. For WS$_2$, the in-plane vibrational E_{2g}^1 mode is redshift from ~ 354 cm^{-1} for 1L to ~ 350 cm^{-1} for 3L, while the out-of-plane A$_{1g}$ mode is at ~ 418 cm^{-1}. For WSe$_2$, the E_{2g}^1 mode is at ~ 250 cm^{-1} and the A$_{1g}$ mode is at ~260 cm^{-1}. These consistency with previous measurements further confirms the quality of the exfoliated sample and the identification of the layer number.
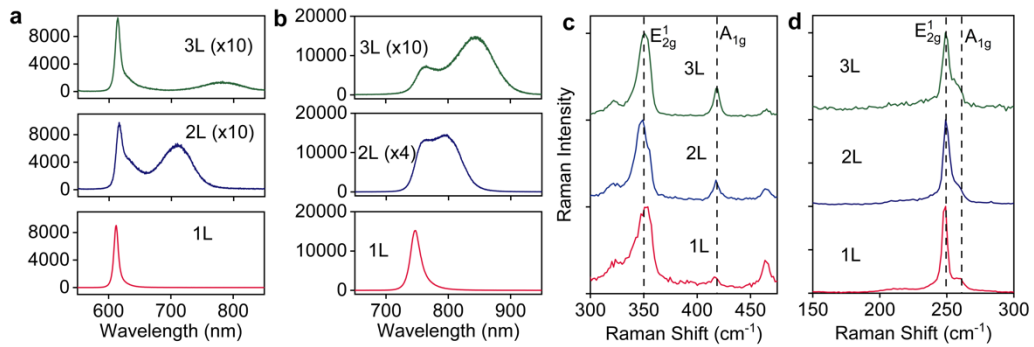

Fig. 2. (a, b) PL intensity of 1L (red), 2L (blue), and 3L (green) WS$_2$ (a) and WSe$_2$ (b) samples. The curvesare offset for clarity. (c, d) Raman spectra of 1L (red), 2L (blue), and 3L (green) WS$_2$ (c) and WSe$_2$ (d) samples.

At the wavelengths around A exciton, the absorption coefficient is significantly increased. Figures 3a-c illustrate the broadband reflectance contrast measurements for 1-layer (1L), 2-layer (2L), and 3-layer (3L) WS$_2$. When increasing the layer number, a slight red-shift of the A exciton peak is observed in the reflectance contrast measurement. This shift is attributed to the narrowing of the bandgap energy when transitioning from monolayer TMDs to

multilayer TMDs, consistent with previous reports [48]. The relation between the reflectance contrast $\Delta R/R$ and the absorption coefficient α_0 is described by the following equations [49] (Supplementary S2):

$$\alpha_0 = \left| \frac{n_0 - 1}{n_0 + 1} \right| \Delta R / R, \tag{1}$$

where n_0 refers to the refractive index of the substrate and it is 1.46 for quartz in our study. Normalized reflection contrast $\Delta R/R$ is around 0.56 (1L), 0.70 (2L), and 1.13 (3L) at the exciton resonance.

To study the power dependency of reflectance contrast of WS_2, we chose five wavelengths across the A exciton peak, with a step of approximately 3 nm, centered at the wavelength of 616.2 nm, 621.5 nm and 624.2 nm, for 1L, 2L and 3L WS_2. The results are demonstrated in Fig. 3d-f. At the peak wavelength (616.2 nm) of the A exciton, $\Delta R/R$ is ~0.45 in the low power density range, close to the value of steady reflectance contrast. As the peak power density increases to around 9.8×10^6 W/cm^2, $\Delta R/R$ decreases to 0.29. On either the red or blue side of the A exciton, the reduction in reflectance contrast is less pronounced within the power density range of our measurements. For example, it decreases from 0.42 to 0.33 for 611.5 nm and from 0.46 to 0.38 for 620.4 nm, respectively. Notably, at 606.2 nm, the change in $\Delta R/R$ increases as the pump power intensity rises, indicating the occurrence of two-photon absorption. At the resonant wavelength of A exciton in 2L and 3L samples, $\Delta R/R$ is approximately 0.71 and 1.11, respectively, in the low power density range, which is also close to the steady reflectance contrast. As the pump wavelength shifts away from the resonant peak, the reduction of $\Delta R/R$ in the power-dependent measurements also becomes less pronounced.
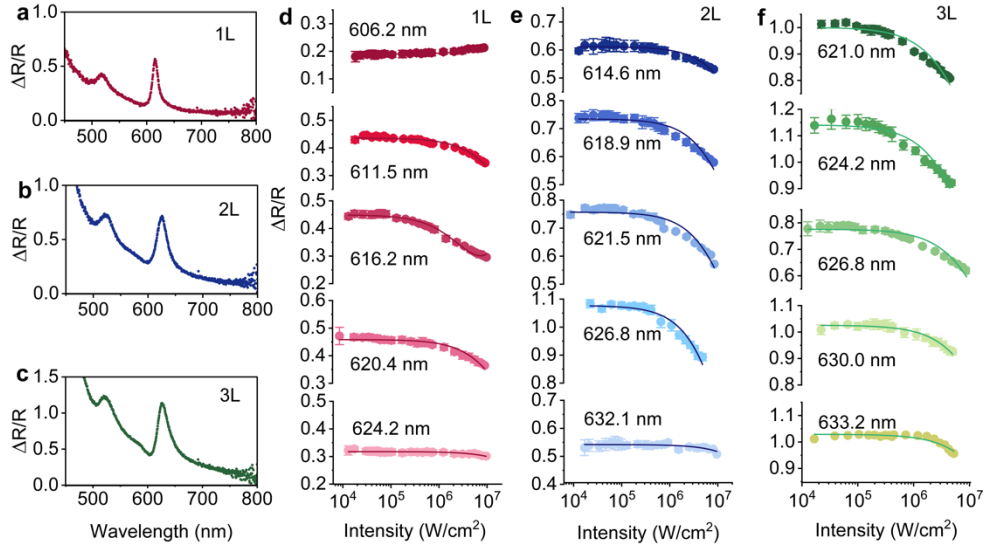
Fig. 3. Steady (a-c) and power-dependent pulsed (d-f) reflectance contrast of 1L, 2L, and 3L WS$_2$ around A exciton resonance. The pumping wavelength is scanned across the exciton resonance. The curves for different pumping wavelengths are vertically shifted for clarity.

Figures 4a-c illustrate the broadband reflectance contrast measurements for 1L, 2L, and 3L WSe$_2$. Normalized reflection contrast $\Delta R/R$ is around 0.48 (1L), 0.58 (2L), and 0.91 (3L) at the exciton resonance. Fig. 4d-f presents the result of power-dependent measurement for 1L, 2L, and 3L WSe$_2$ samples, at the five wavelengths selected across the A exciton peak. For 1L WSe$_2$ at the peak wavelength of A exciton, $\Delta R/R$ is around 0.47 in the low power density range, close to the value of steady reflectance contrast. As the peak power density increases to around 9.6×10^6 W/cm^2, $\Delta R/R$ decreases to ~0.28. When the pump wavelength is shifted to the red or blue side of A exciton, the reduction of reflectance contrast becomes smaller. It decreases from 0.46 to

0.30 at 743 nm and from 0.41 to 0.3 at 749.3 nm. For 2L and 3L WSe$_2$, $\Delta R/R$ is around 0.66 and 0.86 at the peak wavelength of A exciton in the low power density range. As the pump wavelength shifts away from the resonant peak, the reduction of $\Delta R/R$ in the power-dependent measurements also becomes less pronounced, similar to the case in WS$_2$.
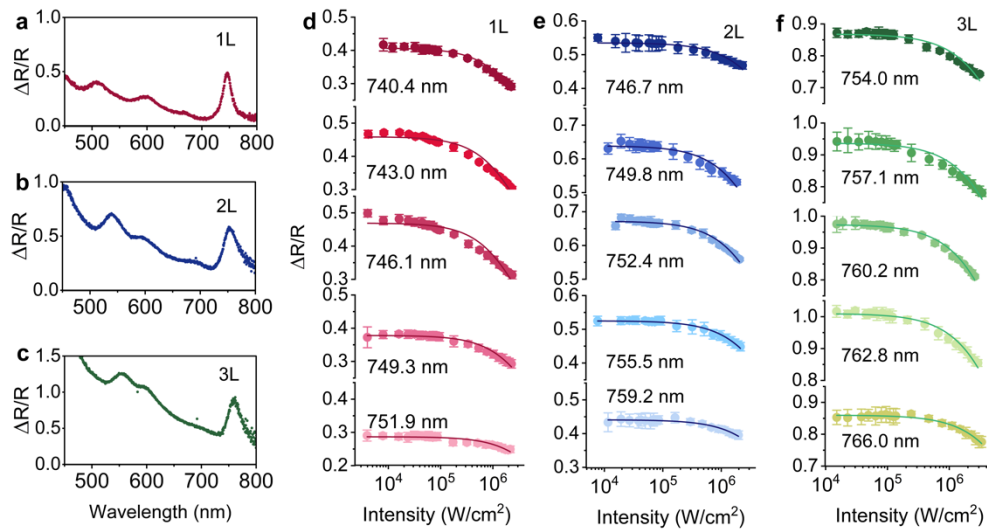

Fig. 4. Steady (a-c) and power-dependent pulsed (d-f) reflectance contrast of 1L, 2L, and 3L WSe$_2$ around A exciton resonance. The pumping wavelength is scanned across the exciton resonance. The curves for different pumping wavelengths are vertically shifted for clarity.

To exclude artifacts from the experiment setup, we repeat the experiments far from the exciton resonance, as shown in Supplementary Fig S2-3. No significant decrease in the reflectance contrast was observed at these wavelengths within the power density range of our measurements. Therefore, we can attribute the decreases in reflectance contrast to the Pauli blocking

effect at the exciton resonance. As the power density increases, the presence of exciton prevents further optical transitions, meaning that the A exciton is bleached. In high-density regimes, exciton-exciton scattering can also be included to explain the decrease in the absorption peak [41]. To extract the threshold intensity of SA and the coefficient of two-photon absorption, we can fit the measured absorption coefficient α according to the following equation [20]

$$\alpha(I) = \frac{\alpha_0}{1 + I/I_s} + \beta I, \tag{2}$$

where I is the pump power density, β is the coefficient of two-photon absorption and I_s is the saturation power density threshold at which the absorption coefficient α is reduced to half of its original value α_0. By fitting the measured reflectance contrast at different pump intensities to Eq. 2, the saturation threshold intensity can be obtained, as shown by the solid lines in Fig. 3d-f and Fig. 4d-f. At the peak wavelength of the A exciton, the saturation threshold intensity is 5.5×10^6, 2.4×10^7 and 2.1×10^7 W/cm^2 for 1L, 2L and 3L WS$_2$, and 3.8×10^6, 8.0×10^6 and 1.2×10^7 W/cm^2, for 1L, 2L and 3L WSe$_2$, respectively. Obviously, the saturation threshold intensity increases with the number of layers. Note that in the fittings, we intentionally set the coefficient of two-photon absorption to zero to obtain the best fit, except at the wavelength of 616.2 nm and 606.2 nm for the 1L WS$_2$ sample. At these specific wavelengths, the influence of two-photon absorption can partially offset the effect of SA and therefore cannot be neglected in the fitting.

To understand the evolution of the saturation threshold I_s around the A-exciton peak, we plot the power density threshold for both WS$_2$ and WSe$_2$ in

Fig. 5. Consistently across all samples, the lowest power density threshold occurs at the wavelength corresponding to the A-exciton resonant peak. For samples with the same layer number, WS_2 exhibits a higher threshold power density than WSe_2. No clear signs of two-photon absorption are observed in the WSe_2 samples in the experimental range of pumping power density, while the appearance of two-photon absorption is clear in the 1L WS_2 sample.
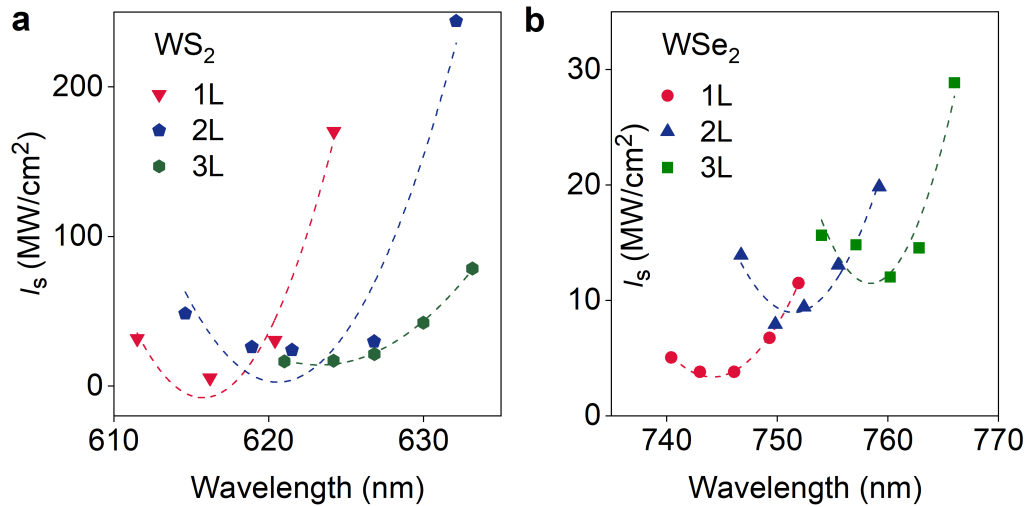

FIG. 5. Comparison of the saturation threshold for few-layer WS_2 and WSe_2. (a) Threshold comparison of few-layer WS_2. (b) Threshold comparison of few-layer WSe_2.

For both WS_2 and WSe_2 samples, the saturation power density threshold increases as the layer number increases. For an incident light of a given power density, the exciton density in thicker layers is lower than that in thinner layers, though the absorption coefficient is higher for thicker layers. For example, comparing the 1L and 2L WS_2, the volume and so the total number of atoms (the total electronic states are proportional to this number) is different by two times, but the difference in the steady absorption coefficient is

obviously smaller, 0.106 vs 0.134, according to Fig. 3a and Eq. 3. Consequently, the multilayer structure is less prone to saturation.

Previous research has demonstrated the layer-dependent saturation threshold for WS_2 at the wavelength of 800 nm, indicating that the saturation threshold decreases with layer number [33]. As shown in Fig. 3a-3c, this change in the saturation threshold is mainly due to the redshift of the exciton resonant wavelength as the layer number increases, approaching the pumping light. According to Fig. 5, the saturation threshold would decrease as the exciton resonant wavelength approaches the pump wavelength, or alternatively, the exciton resonance dominates the NLO saturation behaviors. Comparing the WS_2 and WSe_2, the variance of the saturation threshold of WS_2 is more sensitive to the deviation from the A-exciton resonant peak than that of WSe_2, because the exciton resonance is stronger for WS_2. Compared with previous works using non-resonant excitation, resonant excitation has about two orders of magnitude lower in saturation power density threshold.

3. Theoretical Analysis

A comparison between the saturation intensity and corresponding exciton density in our experiments and previous works is summarized in Table 1. It shows that the saturation intensity varies for different materials, pump wavelengths pulse duration, etc. In this section, we propose a theoretical model to further elucidate the dependence of the saturation power density threshold on the pulse duration.

After light absorption, the exciton density n is generally determined by

[34]:

$$n = \frac{I\tau\alpha}{Nh\nu}\eta \ ,$$

(3)

where τ is the lifetime of the exciton, α is the absorption coefficient of TMDs, N is the number of layers, $h\nu$ is the photon energy of the pump light, and η is the efficiency of generating an exciton when absorbing a single photon, which is close to unity for resonant excitation. As an initial analysis for Eq. 2, the saturation threshold I_s, at which the absorption coefficient drops to one-half, corresponds to a saturation exciton density n_s that is half of the total exciton states available for absorption. Since the total available absorption state is a constant over a certain frequency region, for a given material, the saturation threshold will follow $I_s(\lambda) \sim \alpha^{-1}(\lambda)$. This implies a dip at the exciton resonance if η does not vary significantly over the small spectral range used. This qualitatively explains the reduction of saturation threshold at the exciton peak shown in Fig. 5b. For different layer numbers, though the total absorption increases as the layer number N increases, the volume (thickness) of the layer increases as well. Then, the exciton density decreases considering that the absorption coefficient per unit length α/N decreases for 2L or 3L samples, compared with the monolayer. Therefore, the saturation threshold at exciton resonance increases as the number of layers. Previous studies by z-scan measurement using 100 fs pulses show a clear SA at 800 nm for MoS_2 from liquid-phase exfoliation [20]. The bleaching effect was also reported in broadband pump-probe measurement, where the reduction of the resonant peak in reflectance contrast is remarkable at high pump intensity [36, 41].

Table 1 Comparison of the saturation threshold of few layer TMDs

Sample	Pump wavelength (Repetition Rate, Pulse Duration)	I_s (W/cm^2)	n_s (cm^{-2})	Reference
WS$_2$	1550 nm (37 MHz, 560 fs)	1.48×10^8	NA	[24]
WSe$_2$	1550 nm (37 MHz, 560 fs)	2.7×10^8	NA	[24]
MoS$_2$/CHP	800 nm (1 kHz, 100 fs)	4.05×10^{11}	NA	[20]
21L WS$_2$	800 nm (1 kHz, 35 fs)	2.08×10^{11}	NA	[33]
22L MoS$_2$	800 nm (1 kHz, 35 fs)	5.52×10^{11}	NA	[33]
1L WS$_2$	803 nm (91 MHz, 15ps)	6.86×10^4	NA	[50]
1L MoS$_2$	520 nm (1 kHz, 350 fs)	NA	4.1×10^{12}	[32]
1L MoSe$_2$	520 nm (1 kHz, 350 fs)	NA	6.9×10^{12}	[32]
1L WS$_2$	520 nm (1 kHz, 350 fs)	NA	3.29×10^{12}	[32]
1L WSe$_2$	520 nm (1 kHz, 350 fs)	NA	3.83×10^{12}	[32]
1L WS$_2$	616.2 nm (8.66 MHz, 78 ps)	5.5×10^6	1.1×10^{13}	This work
2L WS$_2$	621.5 nm (8.66 MHz, 78 ps)	2.4×10^7	NA	This work
3L WS$_2$	624.2 nm (8.66 MHz, 78 ps)	2.1×10^7	NA	This work
1L WSe$_2$	743.0 nm (8.66 MHz, 78 ps)	3.8×10^6	6.9×10^{12}	This work
2L WSe$_2$	749.8 nm (8.66 MHz, 78 ps)	8.0×10^6	NA	This work
3L WSe$_2$	760.2 nm (8.66 MHz, 78 ps)	1.2×10^7	NA	This work

To disentangle the contribution of wavelength and pulse duration to the saturation threshold intensity, we solve the empirical dynamics equation of carriers using a pulse excitation. Since the exciton-exciton annihilation effect can be strong at high power densities [32, 51, 52], the exciton dynamics equation including the exciton-exciton annihilation effect could be written as

$$\frac{dn}{dt} = G - \frac{n}{\tau} - \gamma n^2, \tag{4}$$

where $G = I\alpha_0\lambda/hc(1+I/I_S)$ is the generation rate of exciton, γ is the annihilation rate from the exciton-exciton interaction [32]. Considering the pump laser pulse as a square function with a pulse duration τ_p, it follows

$$I(t) = \begin{cases} I_0, & 0 \le t \le \tau_p \\ 0, & t > \tau_p \end{cases}. \tag{5}$$

The analytical solution for Eq. 4 under the condition of Eq.5 could be written as follows:

$$n(t) = \begin{cases} \dfrac{m_0 e^{2B\gamma t}+1}{m_0 e^{2B\gamma t}-1}\sqrt{\dfrac{G}{\gamma}+\dfrac{1}{4\gamma^2\tau^2}} - \dfrac{1}{2\gamma\tau}, & 0 \le t \le t_p \\ \left(\dfrac{2}{q_0 e^{2B\gamma t}-1}\right)\dfrac{1}{2\gamma\tau}, & t > t_p \end{cases}, \tag{6}$$

where m_0 and q_0 are constants determined by the initial exciton density and B is defined as:

$$B = \sqrt{\frac{G}{\gamma}+\frac{1}{4\gamma^2\tau^2}} \tag{7}$$

Eqs. 6-7 describe the dynamics under single pulse excitation. It applies to those cases where the pulse separation, i.e., the reciprocal of the repetition rate of the laser, is much larger than the characteristic time scale of the exciton. If the repetition rate of the laser is high, the analytical solution of Eq. 4 under periodic excitation could be written as

$$n(t) = \begin{cases} \dfrac{m_k e^{2B\gamma t} + 1}{m_k e^{2B\gamma t} - 1} \sqrt{\dfrac{G}{\gamma} + \dfrac{1}{4\gamma^2 \tau^2}} - \dfrac{1}{2\gamma \tau}, & kT \leq t \leq kT + t_{\mathrm{p}} \\[4mm] \left(\dfrac{q_k e^{2B\gamma t} + 1}{q_k e^{2B\gamma t} - 1} - 1 \right) \dfrac{1}{2\gamma \tau}, & kT + t_{\mathrm{p}} < t < kT + T \end{cases} , \qquad (8)$$

where q_k and m_{k+1} are undetermined coefficients for period k and $k+1$. These coefficients could be derived from the recursive relations according to the boundary conditions introduced by the consistency of exciton density:

$$\left(\frac{q_k e^{2B\gamma(kT+t_p)} + 1}{q_k e^{2B\gamma(kT+t_p)} - 1} - 1 \right) \frac{1}{2\gamma\tau} = \frac{m_k e^{2B\gamma(kT+t_p)} + 1}{m_k e^{2B\gamma(kT+t_p)} - 1} \sqrt{\frac{G}{\gamma} + \frac{1}{4\gamma^2\tau^2}} - \frac{1}{2\gamma\tau} , \qquad (9)$$

$$\left(\frac{q_k e^{2B\gamma(k+1)T} + 1}{q_k e^{2B\gamma(k+1)T} - 1} - 1 \right) \frac{1}{2\gamma\tau} = \frac{m_{k+1} e^{2B\gamma(k+1)T} + 1}{m_{k+1} e^{2B\gamma(k+1)T} - 1} \sqrt{\frac{G}{\gamma} + \frac{1}{4\gamma^2\tau^2}} - \frac{1}{2\gamma\tau} . \qquad (10)$$

Fig. 6a demonstrates the dynamics of transient exciton density under different pulse duration in 1L WS$_2$ according to Eqs. 8-10. The laser repetition rate is set to 8.66 MHz, consistent with our experimental parameters, and the pump intensities are 5.5 MW/cm^2 for WS$_2$ and 3.8 MW/cm^2 for WSe$_2$, respectively. The lifetime of the exciton τ and the annihilation rate from the exciton-exciton interaction γ of WS$_2$ and WSe$_2$ (τ = 124.665 ps, γ = 0.016 cm^2/s for 1L WS$_2$; τ = 115.8 ps, γ = 0.026 cm^2/s for 1L WSe$_2$) are taken from Ref. [32]. Based on these parameters, the estimated saturation exciton densities are 1.1×10^{13} for 1L WS$_2$ and 6.9×10^{12} cm^{-2} for 1L WSe$_2$.

For larger pulse durations, the exciton density does not increase over the entire pulse duration but saturates because of the strong exciton-exciton annihilation process at high exciton densities. From the curves, the characteristic rising (decay) time of the exciton density can be determined to be 5.49 ps (13.5 ps), corresponding mostly to the exciton-exciton interaction

strength. For very short pulses, the total energy per pulse is insufficient to pump the sample to reach the threshold exciton density. In this case, the nonlinearity from the materials will be much weaker even though the peak intensity of the pump has reached the threshold intensity.

Fig. 6b illustrates the influence of the pulse duration on the transient exciton density in 1L WS_2 under constant single pulse energy. Shorter pulses have higher peak power density compared to longer pulses, enabling a higher exciton generation rate and making it easier to reach the saturation exciton density threshold. However, the pulse duration must also align with the characteristic timescale of the material, specifically the rising time of exciton density (5.49 ps for 1L WS_2, as determined earlier). For pulse durations much shorter than this characteristic rising time, the peak exciton density decreases significantly because the material cannot absorb sufficient light before the excitons are annihilated. In contrast, for pulse durations longer than the characteristic rising time, shorter pulses result in a larger peak exciton density. This is due to the dynamic balance between exciton creation via light absorption and exciton annihilation during longer pulses, which limits the peak exciton density.

This analysis also explains the observed differences between our measured saturation peak power density using a picosecond pulsed laser and previous measurements with femtosecond lasers [24, 32, 33, 50]. The significantly shorter pulse durations in femtosecond experiments fall well below the characteristic rising time of exciton density. Consequently, higher pump intensities are required to compensate for the insufficient pulse duration, resulting in a higher observed saturation peak power density in those
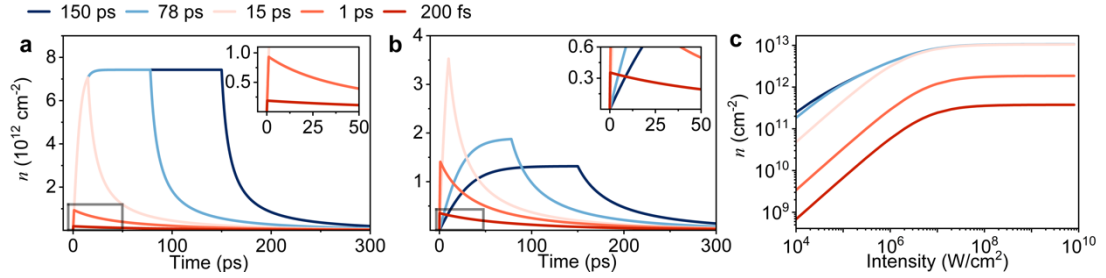
experiments.

FIG. 6. The evolution of exciton density in monolayer WS_2 for different pulse durations. (a) Transient dynamics of exciton density under constant pump intensity. (b) Transient dynamics of exciton density under constant single pulse energy (17.16 $\mu J/cm^2$). The insets in (a, b) shows an enlarged view of the gray box. (c) The evolution of peak exciton density under various pump fluences. The threshold intensity I_s is assumed to be 5.5×10^6 W/cm^2 corresponding to 1L WS_2.

We can also calculate the peak exciton density for monolayer WS_2 as a function of peak pump intensity for different pulse durations, as shown in Fig. 6c. It is clear that the exciton density can always reach a maximum under different pulse durations. But only when the pulse duration is large enough compared with the characteristic time scale of the material can the maximum approach its limit. As depicted in Fig. 6c, the estimated saturation exciton density for 1L WS_2 reaches approximately 10^{12} cm^{-2} under the pulse duration of 78 ps, consistent with thresholds reported in Ref [32]. The material saturates at a lower exciton density yet higher pump intensity under shorter pulse durations. As the pulse duration increases, the saturation exciton density saturates at a certain level as a result of the strong exciton-exciton annihilation effect. The extended discussion here aims to explain that with longer pulse

durations, the high exciton density state occupies a longer transient scale, hence more easily reaching saturation. Simultaneously, while the peak exciton density increases with pulse width, this increase is not unbounded due to the impracticality of excessively high exciton densities, which would surpass the Mott transition threshold.

Fig. 6 also implies guidelines for the choice of laser parameters in measuring the saturation threshold, especially the pulse duration. If the single pulse energy is significantly large, a longer pulse duration is better to observe the nonlinearity of the material. On the contrary, very short pulses lead to unbleached samples because of the slow accumulation of the exciton density. If single pulse energy is limited to a low level, one should choose a shorter pulse to reach the threshold intensity of the material. A preferred option is pulse duration comparable to the characteristic time scale of the exciton, then the peak exciton density can reach as high as possible for a limited single pulse energy.

4. Conclusion

In summary, we carried power-dependent measurements on 1~3 layer WS_2 and WSe_2, extracting the saturation threshold as a function of pumping wavelength. For both WS_2 and WSe_2, the power density threshold is minimized at the wavelength corresponding to the A-exciton resonant. At the resonance wavelength, the saturation threshold in both WS_2 and WSe_2 escalates with an increase in the number of layers. The analytical solution to the dynamics equation reveals the ultrafast dynamics of exciton density under different pulse durations. It implies that the choice of pulse duration plays a crucial role in observing the saturation threshold and the nonlinearity of the

material. Specifically, longer pulse durations are beneficial for significantly large single pulse energy, while shorter pulses are more effective in reaching the threshold intensity if the single pulse energy is limited. Our results contribute valuable insights into the design of TMD-based active optical devices and highlight the importance of laser parameters when exploring the $\chi^{(3)}$ nonlinearity of optical materials.

Disclosures

The authors declare no conflicts of interest.

Data Availablity Statement

Data underlying the results presented in this paper are not publicly available at

this time but may be obtained from the authors upon reasonable request.

Supplementary Materials

See Supplement 1 for supporting content.

References

[1] S.Z. Butler, S.M. Hollen, L. Cao, Y. Cui, J.A. Gupta, H.R. Gutiérrez, T.F. Heinz, S.S. Hong, J. Huang, A.F. Ismach, Progress, challenges, and opportunities in two-dimensional materials beyond graphene, ACS Nano, 7 (2013) 2898-2926.

[2] A.K. Geim, K.S. Novoselov, The rise of graphene, Nature Materials, 6 (2007) 183-191.

[3] B. Munkhbat, B. Küçüköz, D.G. Baranov, T.J. Antosiewicz, T.O. Shegai, Nanostructured transition metal dichalcogenide multilayers for advanced nanophotonics, Laser & Photonics Reviews, 17 (2023) 2200057.

[4] Q.H. Wang, K. Kalantar-Zadeh, A. Kis, J.N. Coleman, M.S. Strano, Electronics and optoelectronics of two-dimensional transition metal dichalcogenides, Nature Nanotechnology, 7 (2012) 699-712.

[5] J.R. Schaibley, H. Yu, G. Clark, P. Rivera, J.S. Ross, K.L. Seyler, W. Yao, X. Xu, Valleytronics in 2D materials, Nature Reviews Materials, 1 (2016) 1-15.

[6] T. Fryett, A. Zhan, A. Majumdar, Cavity nonlinear optics with layered materials, Nanophotonics, 7 (2017) 355-370.

[7] Q. Bao, H. Zhang, Y. Wang, Z. Ni, Y. Yan, Z.X. Shen, K.P. Loh, D.Y. Tang, Atomic‐layer graphene as a saturable absorber for ultrafast pulsed lasers, Advanced Functional Materials, 19 (2009) 3077-3083.

[8] Q. Bao, H. Zhang, Z. Ni, Y. Wang, L. Polavarapu, Z. Shen, Q.-H. Xu, D. Tang, K.P. Loh, Monolayer graphene as a saturable absorber in a mode-locked laser, Nano Research, 4 (2011) 297-307.

[9] D. Popa, Z. Sun, F. Torrisi, T. Hasan, F. Wang, A. Ferrari, Sub 200 fs pulse generation from a graphene mode-locked fiber laser, Applied Physics Letters, 97 (2010) 203106.

[10] J. Sotor, I. Pasternak, A. Krajewska, W. Strupinski, G. Sobon, Sub-90 fs a stretched-pulse mode-locked fiber laser based on a graphene saturable absorber, Optics Express, 23 (2015) 27503-27508.

[11] Z. Sun, T. Hasan, F. Torrisi, D. Popa, G. Privitera, F. Wang, F. Bonaccorso, D.M. Basko, A.C. Ferrari, Graphene mode-locked ultrafast laser, ACS Nano, 4 (2010) 803-810.

[12] Z. Sun, D. Popa, T. Hasan, F. Torrisi, F. Wang, E.J. Kelleher, J.C. Travers, V. Nicolosi, A.C. Ferrari, A stable, wideband tunable, near transform-limited, graphene-mode-locked, ultrafast laser, Nano Research, 3 (2010) 653-660.

[13] Q. Bao, H. Zhang, J.x. Yang, S. Wang, D.Y. Tang, R. Jose, S. Ramakrishna, C.T. Lim, K.P. Loh, Graphene–polymer nanofiber membrane for ultrafast photonics, Advanced Functional Materials, 20 (2010) 782-791.

[14] H. Zhang, Q. Bao, D. Tang, L. Zhao, K. Loh, Large energy soliton erbium-doped fiber laser with a graphene-polymer composite mode locker, Applied Physics Letters, 95 (2009).

[15] E.J. Lee, S.Y. Choi, H. Jeong, N.H. Park, W. Yim, M.H. Kim, J.-K. Park, S. Son, S. Bae, S.J. Kim, Active control of all-fibre graphene devices with electrical gating, Nature Communications, 6 (2015) 6851.

[16] O. Kovalchuk, S. Uddin, S. Lee, Y.-W. Song, Graphene capacitor-based electrical switching of mode-locking in all-fiberized femtosecond lasers, ACS Applied Materials & Interfaces, 12 (2020) 54005-54011.

[17] K. Chen, X. Zhou, X. Cheng, R. Qiao, Y. Cheng, C. Liu, Y. Xie, W. Yu, F. Yao, Z. Sun, Graphene photonic crystal fibre with strong and tunable light–matter interaction, Nature Photonics, 13 (2019) 754-759.

[18] R.I. Woodward, E.J. Kelleher, 2D saturable absorbers for fibre lasers, Applied Sciences, 5 (2015) 1440-1456.

[19] C. Ma, C. Wang, B. Gao, J. Adams, G. Wu, H. Zhang, Recent progress in ultrafast lasers based on 2D materials as a saturable absorber, Applied Physics Reviews, 6 (2019).

[20] K. Wang, J. Wang, J. Fan, M. Lotya, A. O'Neill, D. Fox, Y. Feng, X. Zhang, B. Jiang, Q. Zhao, Ultrafast saturable absorption of two-dimensional MoS_2 nanosheets, ACS Nano, 7 (2013) 9260-9267.

[21] S. Bikorimana, P. Lama, A. Walser, R. Dorsinville, S. Anghel, A. Mitioglu, A. Micu, L. Kulyuk, Nonlinear optical responses in two-dimensional transition metal dichalcogenide multilayer: WS_2, WSe_2, MoS_2 and $Mo_{0.5}W_{0.5}S_2$, Optics Express, 24 (2016) 20685-20695.

[22] Y. Li, N. Dong, S. Zhang, X. Zhang, Y. Feng, K. Wang, L. Zhang, J. Wang, Giant two-photon absorption in monolayer MoS_2, Laser & Photonics Reviews, 9 (2015) 427-434.

[23] R. Woodward, R. Howe, T. Runcorn, G. Hu, F. Torrisi, E. Kelleher, T. Hasan, Wideband saturable absorption in few-layer molybdenum diselenide (MoSe 2) for Q-switching Yb-, Er- and Tm-doped fiber lasers, Optics Express, 23 (2015) 20051-20061.

[24] S. Zhang, N. Dong, N. McEvoy, M. O'Brien, S. Winters, N.C. Berner, C. Yim, Y. Li, X. Zhang, Z. Chen, Direct observation of degenerate two-photon absorption and its saturation in WS_2 and MoS_2 monolayer and few-layer films, ACS Nano, 9 (2015) 7142-7150.

[25] B. Chen, X. Zhang, K. Wu, H. Wang, J. Wang, J. Chen, Q-switched fiber laser based on transition metal dichalcogenides MoS_2, $MoSe_2$, WS_2, and WSe_2, Optics Express, 23 (2015) 26723-26737.

[26] K. Wang, Y. Feng, C. Chang, J. Zhan, C. Wang, Q. Zhao, J.N. Coleman, L. Zhang, W.J. Blau, J. Wang, Broadband ultrafast nonlinear absorption and nonlinear refraction of layered molybdenum dichalcogenide semiconductors, Nanoscale, 6 (2014) 10530-10535.

[27] G. Wang, G. Liang, A.A. Baker-Murray, K. Wang, J.J. Wang, X. Zhang, D. Bennett, J.-T. Luo, J. Wang, P. Fan, Nonlinear optical performance of few-layer molybdenum diselenide as a slow-saturable absorber, Photonics Research, 6 (2018) 674-680.

[28] K. Wu, X. Zhang, J. Wang, X. Li, J. Chen, WS_2 as a saturable absorber for ultrafast photonic applications of mode-locked and Q-switched lasers, Optics Express, 23 (2015) 11453-11461.

[29] M. Zhang, G. Hu, G. Hu, R. Howe, L. Chen, Z. Zheng, T. Hasan, Yb-and Er-doped fiber laser Q-switched with an optically uniform, broadband WS_2 saturable absorber, Scientific Reports, 5 (2015) 17482.

[30] K. Surbhi, S. Bhakta, A. Kumari, U.P. Sahoo, P.K. Sahoo, R. Das, Impact of pauli-blocking effect on optical limiting properties of WSe_2 thin films, Optical Materials, 129 (2022) 112479.

[31] M. Khanzadeh, S. Marashi, Laser beam intensity and wavelength dependent nonlinear absorption in pulse laser deposited WS_2 thin films, Optical Materials, 127 (2022) 112249.

[32] T. Zhang, J. Wang, Defect-enhanced exciton–exciton annihilation in monolayer transition metal dichalcogenides at high exciton densities, ACS Photonics, 8 (2021) 2770-2780.

[33] C. Lu, M. Luo, Y. Ge, Y. Huang, Q. Zhao, Y. Zhou, X. Xu, Layer-dependent nonlinear optical properties of WS_2, MoS_2, and Bi_2S_3 films synthesized by chemical vapor deposition, ACS Applied Materials & Interfaces, 14 (2021) 2390-2400.

[34] A. Chernikov, C. Ruppert, H.M. Hill, A.F. Rigosi, T.F. Heinz, Population inversion and giant bandgap renormalization in atomically thin WS_2 layers, Nature Photonics, 9 (2015) 466-470.

[35] C. Ruppert, A. Chernikov, H.M. Hill, A.F. Rigosi, T.F. Heinz, The role of electronic and phononic excitation in the optical response of monolayer WS_2 after ultrafast excitation, Nano Letters, 17 (2017) 644-651.

[36] C. Trovatello, F. Katsch, Q. Li, X. Zhu, A. Knorr, G. Cerullo, S. Dal Conte, Disentangling many-body effects in the coherent optical response of 2D semiconductors, Nano Letters, 22 (2022) 5322-5329.

[37] H. Wang, C. Zhang, F. Rana, Ultrafast dynamics of defect-assisted electron–hole recombination in monolayer MoS_2, Nano Letters, 15 (2015) 339-345.

[38] D. Erkensten, S. Brem, E. Malic, Exciton-exciton interaction in transition metal dichalcogenide monolayers and van der Waals heterostructures, Physical Review B, 103 (2021) 045426.

[39] E.A. Pogna, M. Marsili, D. De Fazio, S. Dal Conte, C. Manzoni, D. Sangalli, D. Yoon, A. Lombardo, A.C. Ferrari, A. Marini, Photo-induced bandgap renormalization governs the

ultrafast response of single-layer MoS_2, ACS Nano, 10 (2016) 1182-1188.

[40] R. Schmidt, G. Berghauser, R. Schneider, M. Selig, P. Tonndorf, E. Malic, A. Knorr, S. Michaelis de Vasconcellos, R. Bratschitsch, Ultrafast coulomb-induced intervalley coupling in atomically thin WS_2, Nano letters, 16 (2016) 2945-2950.

[41] F. Katsch, M. Selig, A. Knorr, Exciton-scattering-induced dephasing in two-dimensional semiconductors, Physical Review Letters, 124 (2020) 257402.

[42] A. Kavokin, T.C.H. Liew, C. Schneider, P.G. Lagoudakis, S. Klembt, S. Hoefling, Polariton condensates for classical and quantum computing, Nature Reviews Physics, 4 (2022) 435-451.

[43] G. Muñoz-Matutano, A. Wood, M. Johnsson, X. Vidal, B.Q. Baragiola, A. Reinhard, A. Lemaître, J. Bloch, A. Amo, G. Nogues, B. Besga, M. Richard, T. Volz, Emergence of quantum correlations from interacting fibre-cavity polaritons, Nature Materials, 18 (2019) 213-218.

[44] J. Yin, J. Li, H. Chen, J. Wang, P. Yan, M. Liu, W. Liu, W. Lu, Z. Xu, W. Zhang, Large-area highly crystalline WSe_2 atomic layers for ultrafast pulsed lasers, Optics Express, 25 (2017) 30020-30031.

[45] K.S. Novoselov, A.K. Geim, S.V. Morozov, D.-e. Jiang, Y. Zhang, S.V. Dubonos, I.V. Grigorieva, A.A. Firsov, Electric field effect in atomically thin carbon films, Science, 306 (2004) 666-669.

[46] K. Choi, Y.T. Lee, S.-W. Min, H.S. Lee, T. Nam, H. Kim, S. Im, Direct imprinting of MoS_2 flakes on a patterned gate for nanosheet transistors, Journal of Materials Chemistry C, 1 (2013) 7803-7807.

[47] H. Zeng, G.-B. Liu, J. Dai, Y. Yan, B. Zhu, R. He, L. Xie, S. Xu, X. Chen, W. Yao, Optical signature of symmetry variations and spin-valley coupling in atomically thin tungsten dichalcogenides, Scientific Reports, 3 (2013) 1608.

[48] W. Zhao, Z. Ghorannevis, L. Chu, M. Toh, C. Kloc, P.-H. Tan, G. Eda, Evolution of electronic structure in atomically thin sheets of WS_2 and WSe_2, ACS Nano, 7 (2013) 791-797.

[49] Y. Li, T.F. Heinz, Two-dimensional models for the optical response of thin films, 2D Materials, 5 (2018) 025021.

[50] Q. Hao, K. Ye, M. Dong, J. Liu, Z. Liu, Nonlinear optical response of a monolayer WS_2 and the application of a hundred-MHz nanosecond laser, Optics Express, 29 (2021) 36634-36643.

[51] Y. Yu, Y. Yu, C. Xu, A. Barrette, K. Gundogdu, L. Cao, Fundamental limits of exciton-exciton annihilation for light emission in transition metal dichalcogenide monolayers, Physical Review B, 93 (2016) 201111.

[52] L. Yuan, L. Huang, Exciton dynamics and annihilation in WS_2 2D semiconductors, Nanoscale, 7 (2015) 7402-7408.